

# Self-Epitaxial Hetero-Nanolayers and Surface Atom Reconstruction in Electrocatalytic Nickel Phosphides

Xian-Kui Wei,\* Dehua Xiong, Lifeng Liu, and Rafal E. Dunin-Borkowski

Cite This: *ACS Appl. Mater. Interfaces* 2020, 12, 21616–21622

Read Online

ACCESS |

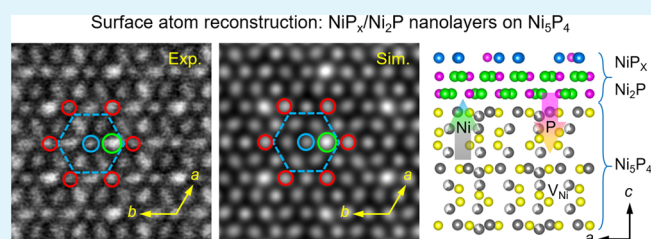
Metrics &amp; More

Article Recommendations

Supporting Information

**ABSTRACT:** Surface atomic, compositional, and electronic structures play decisive roles in governing the performance of catalysts during electrochemical reactions. Nevertheless, for efficient and cheap transition-metal phosphides used for water splitting, such atomic-scale structural information is largely missing. Despite much effort being made so far, there is still a long way to go for establishing a precise structure–activity relationship. Here, in combination with electron-beam bombardment and compositional analysis, our atomic-scale transmission electron microscopy study on  $\text{Ni}_5\text{P}_4$  nanosheets, with a preferential (001) orientation, directly reveals the coverage of a self-epitaxial  $\text{Ni}_2\text{P}$  nanolayer on the phosphide surface. Apart from the presence of nickel vacancies in the  $\text{Ni}_5\text{P}_4$  phase, our quantum-mechanical image simulations also suggest the existence of an additional  $\text{NiP}_x$  ( $0 < x < 0.5$ ) nanolayer, characteristic of complex surface atom reconstruction, on the outermost surface of the phosphides. The surface chemical gradient and the core–shell scenario, probably responsible for the passivated catalytic activity, provide a novel insight to understand the catalytic performance of transition-metal catalysts used for electrochemical energy conversion.

**KEYWORDS:** nickel phosphide, surface reconstruction, transmission electron microscopy, core–shell, water splitting, electron-beam bombardment



## INTRODUCTION

Sustainable production of chemical fuels through electrochemical reactions provides a promising solution for renewable energy storage and usage. Given the scarcity of ideal catalysts, usually precious metals, searching for highly efficient, active, and cheap transition-metal catalysts such as carbides, phosphides, and sulfides becomes one of the urgent tasks.<sup>1,2</sup> In recent years, transition-metal phosphides<sup>3</sup> such as  $\text{Ni}_2\text{P}$ ,  $\text{CoP}$ ,  $\text{FeP}$ , and  $\text{MoP}$  have been reported to possess exceptional activity, efficiency, and stability for water splitting,<sup>4–12</sup> hydrodesulfurization,<sup>13</sup> and  $\text{CO}_2$  reduction.<sup>14</sup> Compared with rapidly developed performance research, nevertheless, atomic-scale structural investigation using experiments is severely delayed or even overlooked.<sup>15,16</sup> Despite tremendous efforts from many pioneering works,<sup>17–19</sup> a long way is still ahead toward realizing rational design of robust catalysts.

Unveiling the surface atomic structure plays a key role in understanding the catalytic pathways for energy conversion.<sup>20,21</sup> Taking two-dimensional (2D)  $\text{MoS}_2$  as an example, its basal plane engineered by surface defects was found to be highly active for the hydrogen evolution reaction (HER). Associated with transmission electron microscopy (TEM) characterization, it is shown that the superior activity is attributed to strained S-vacancies with tunability of the catalytic sites.<sup>22,23</sup> Besides deliberate exposure of the active sites,<sup>24</sup> appropriate surface sulfur doping on  $\text{Ni}_5\text{P}_4$  and

$\text{MoP}$ <sup>25–28</sup> also shows an obvious improvement in performance of the catalysts. However, different from typical 2D materials, these transition-metal catalysts usually have a three-dimensional (3D) morphology. On the nanometer scale, determining their 3D atomic structure, for example, atomic arrangement and species on the surfaces, is very challenging. Therefore, our current understanding of the catalytic mechanism relies more on theoretical models.<sup>17–19,29,30</sup>

With respect to the  $\text{Ni}_2\text{P}$  phase,<sup>7,9</sup> a general argument drawn from theoretical<sup>18</sup> and experimental<sup>10,31,32</sup> studies shows that the  $\text{Ni}_5\text{P}_4$  phase possesses superior catalytic activity for hydrogen production. Nevertheless, except the results from Laursen *et al.*,<sup>7,10</sup> there have been no other results reporting that the performance of  $\text{Ni}_5\text{P}_4$  phase is comparable to that of Pt catalyst. Associated with a survey of the Ni/P composition ratio, the catalytic performance of the pure  $\text{Ni}_5\text{P}_4$  phase relating to the precursors, synthesis methods, and electrolytes is summarized in Table 1. It is seen that phosphorus tends to be enriched in the  $\text{Ni}_5\text{P}_4$  microparticles that possess the best

Received: February 20, 2020

Accepted: April 17, 2020

Published: April 17, 2020

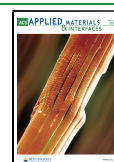


**Table 1.** List of the Compositional Ratios, Precursors, Synthesis Methods, Electrolytes, and Electrocatalytic Activity of Ni<sub>5</sub>P<sub>4</sub> for the HER<sup>a</sup>

morphology, Ni/P ratio	precursors, synthesis method	electrolytes for HER	Tafel slope (mV dec <sup>-1</sup> )	$\eta_{j=10\text{mAcm}^{-2}}$ , mV	ref
microparticle, 1.19 <sup>b</sup>	nickel, red P, solid state reaction	0.5 M H <sub>2</sub> SO <sub>4</sub>	30	43	7
		1 M NaOH	121	193	
microparticle, 1.19	solvothetical, solid state reaction	1 M H <sub>2</sub> SO <sub>4</sub>	33	23	10
		base	98	49	
film, 1.32/1.16 <sub>ICP</sub> <sup>c</sup>	Ni foil, red P, contact-conversion	0.5 M H <sub>2</sub> SO <sub>4</sub>	40	140	8
		1.0 M KOH	53	150	
nanocrystal, 1.33	Ni(acac) <sub>2</sub> , TOP, thermal decomposition	0.5 M H <sub>2</sub> SO <sub>4</sub>	42	118	31
nanosheet, 1.25 <sup>d</sup>	Ni foil/foam, chemical vapor deposition	0.5 M H <sub>2</sub> SO <sub>4</sub>	34	114	32
nanosheet <sup>e</sup> , 1.45	Ni foam, red P, vapor solid reaction	0.5 M H <sub>2</sub> SO <sub>4</sub>	53	108	this work

<sup>a</sup>The atomic ratio of Ni/P mainly obtained from the EDX analysis. <sup>b</sup>The available composition is only from the post-tested Ni<sub>5</sub>P<sub>4</sub> MPs. <sup>c</sup>ICP: inductively coupled plasma optical emission spectrometry. <sup>d</sup>The ratio measured from the EDX line profiles shown in Figure 2 therein is Ni/P = 1.34. <sup>e</sup>The Ni<sub>5</sub>P<sub>4</sub> phase coexists with the Ni<sub>2</sub>P phase.

HER activity, which is supported by density functional theory calculations.<sup>17,18</sup> While for other sample forms, for example, films, nanocrystals, and nanosheets, Ni tends to be enriched on the Ni<sub>5</sub>P<sub>4</sub> phase and leads to the inferior activity.

In this work, to better configure the structure–activity relationship, we investigate the atomic structures of the (001)-oriented Ni<sub>5</sub>P<sub>4</sub> nanosheets, synthesized by vapor phosphorization of the Ni foam,<sup>5</sup> using atomic-resolution scanning/TEM (S/TEM). Our study reveals that the surface structures of the Ni<sub>5</sub>P<sub>4</sub> nanosheets are much more complex than our traditional cognition. Being consistent with the compositional analysis, our electron-beam irradiation experiments directly reveal a self-epitaxial Ni<sub>2</sub>P nanolayer on top of Ni<sub>5</sub>P<sub>4</sub>. Based on quantum mechanical image simulations, a Ni<sub>x</sub> (0 < x < 0.5) nanolayer was found to reconstruct on surfaces of the Ni<sub>2</sub>P-covered Ni<sub>5</sub>P<sub>4</sub> matrix, in which the nickel is suggested to be deficient at specific atomic sites. The structure–activity relation exposed here presents a novel insight toward understanding the catalytic performance of the nickel phosphide catalysts.

## EXPERIMENTAL SECTION

**Sample Preparation and Electrochemical Test.** The phosphide nanosheets were synthesized by direct phosphorization of the commercially available Ni foam at 500 °C for 6 h in a tube furnace. X-ray diffraction analysis shows that the Ni<sub>5</sub>P<sub>4</sub> and Ni<sub>2</sub>P phase takes about 80 and 20% proportion, respectively.<sup>5</sup> As for the TEM specimen preparation, the nanosheets were first scraped using a blade and dispersed in the ultrapure water. By dropping the suspension solution onto copper grid, the prepared TEM specimen was then dried on a plate oven (~60 °C) at ambient conditions and cooled down to room temperature. The HER tests were carried out at room temperature (~25 °C) in a three-electrode cell in 0.5 M H<sub>2</sub>SO<sub>4</sub> solution (pH = 0.28), during which the N<sub>2</sub> bubbling was maintained throughout the experiments. More relevant details are presented elsewhere.<sup>5</sup>

**Electron Microscopy Imaging Experiments.** Scanning electron microscopy (SEM, JEOL, JSM-7400F) was used for sample morphology analysis. An image-corrected FEI Titan 80-300 microscope, with a point resolution better than 80 pm, was operated at 300 kV and used for TEM imaging experiments. An FEI Titan 80-200 Chemi STEM microscope, equipped with a Super-X energy dispersive X-ray spectrometer and bright-field/dark-field STEM detectors, was employed to collect the high-angle annular-dark-field (HAADF) images and the energy dispersive X-ray spectroscopy (EDX) results. The selected area electron diffraction experiments were performed on an FEI Tecnai F20 microscope. During our electron-beam bombardment experiments, a relatively low electron-beam dose rate was used for illuminating thin regions of the phosphide nanosheets.

**Image Simulations.** The CrystalKit-MacTempas software package was used for TEM image simulations, in which the imaging parameters are determined to be C<sub>s</sub> = -10 μm, A<sub>1</sub> = 2.5 nm, and A<sub>2</sub> = B<sub>2</sub> = 90 nm, respectively. The Dr. Probe<sup>33</sup> software package was used for STEM image simulations. Being consistent with the experimental conditions, the collection angle range for the HAADF image simulations was set at 70–200 mrad. Meanwhile, different gap distances between the superimposed sublayers were tested to identify their influence on the column intensity, in which a sublayer spacing of ~0.183 nm was used for our HAADF image simulations.

## RESULTS AND DISCUSSION

The hexagonal Ni<sub>5</sub>P<sub>4</sub>, with lattice parameters  $a_{54} = b_{54} = 0.6789$  nm and  $c_{54} = 1.0989$  nm,<sup>34</sup> is comprised of independent Ni<sub>3</sub>P<sub>3</sub>, Ni<sub>4</sub>P<sub>3</sub>, and Ni<sub>3</sub>P<sub>2</sub> sublayers (Figure 1a), and the screw 6<sub>3</sub>

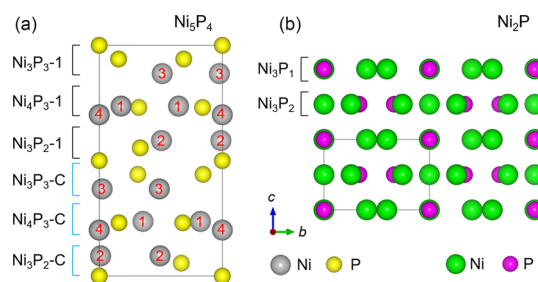


**Figure 1.** Crystal structures of heterogeneous nickel phosphides. (a) [100]-oriented Ni<sub>5</sub>P<sub>4</sub> phase (space group *P6<sub>3</sub>mc*) with labeling the sublayer stacking sequences and Ni atomic sites (Ni1, Ni2, Ni3, and Ni4) within the unit cell. (b) [100]-oriented Ni<sub>2</sub>P phase (space group *P6<sub>2</sub>m*) with labeling the sublayer stacking sequences along the *c* axis.

symmetry leads to their repetition with rotation along the *c* axis. For the hexagonal Ni<sub>2</sub>P phase,<sup>21</sup> it is comprised of stacking Ni<sub>3</sub>P<sub>1</sub> and Ni<sub>3</sub>P<sub>2</sub> sublayers along the *c* axis (Figure 1b). Figure 2a shows the morphology of the Ni<sub>5</sub>P<sub>4</sub> nanosheets grown on the Ni foam, which are several micrometers in the basal plane. Our statistical observations reveal that the nanosheets are preferentially oriented along the [001] direction (Figure S1). By performing EDX detection, our statistical analysis reveals that Ni is enriched on almost all Ni<sub>5</sub>P<sub>4</sub> nanosheets. In the as-grown state, the atomic ratio Ni/P is about 1.45:1, and this ratio decreases to 1.34:1 after the HER test in sulfuric acid for 5 h, which is still higher than the nominal ratio of 1.25:1 (Figure 2b).

Figure 2c shows an atomically resolved TEM image recorded under the negative spherical-aberration imaging

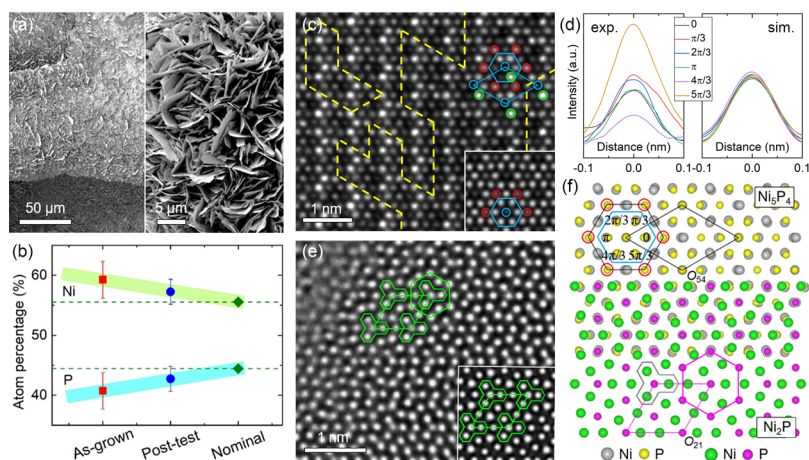


**Figure 2.** Self-epitaxial growth of  $\text{Ni}_2\text{P}$  layers on surfaces of the  $\text{Ni}_5\text{P}_4$  nanosheets. (a) SEM image of the  $\text{Ni}_x\text{P}_y$  nanosheets and an enlarged view (inset). (b) Composition of the as-grown (red), HER-tested (blue)  $\text{Ni}_5\text{P}_4$  nanosheets compared with the nominal stoichiometry (green). (c) Atomic-resolution TEM image of  $\text{Ni}_5\text{P}_4$  recorded along the  $[001]$  direction and the simulated image (thickness  $t = 6.2$  nm). The yellow-dashed lines denote the atomic terraces resulting from surface reconstruction (Figure S2). (d) Intensity profile comparison for the ncNP columns between the experimental and simulated images. (e) Atomic-resolution self-epitaxial  $\text{Ni}_2\text{P}$  phase revealed by electron-beam irradiation on the  $\text{Ni}_5\text{P}_4$  nanosheet and simulated image ( $t = 3.0$  nm) along the  $[001]$  direction. (f) Lattice match relation between the  $\text{Ni}_5\text{P}_4$  and  $\text{Ni}_2\text{P}$  phases along their common  $[001]$  direction. The PUC and ETUC of the  $\text{Ni}_5\text{P}_4$  and  $\text{Ni}_2\text{P}$  phases are denoted by black and pink polygons, respectively.

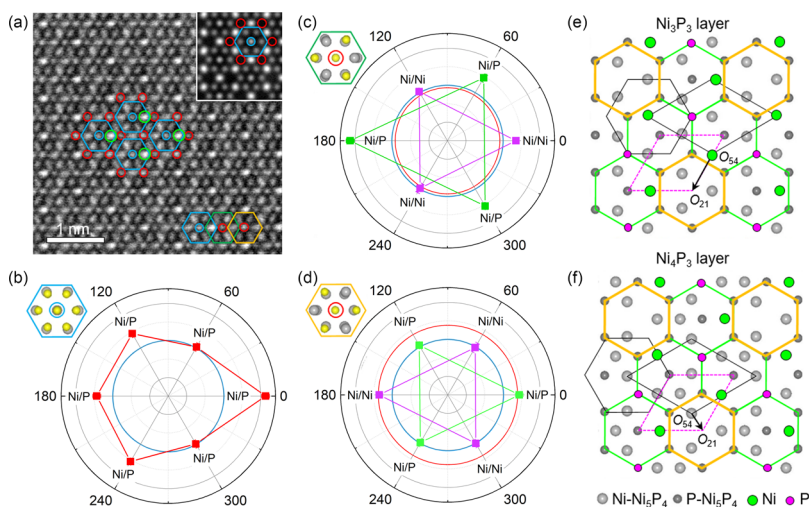


**Figure 3.** Termination-dependent reconstruction of  $\text{Ni}_2\text{P}$  on top of  $\text{Ni}_5\text{P}_4$ . (a) Atomic-resolution HAADF-STEM image of  $\text{Ni}_5\text{P}_4$  collected along the  $[001]$  direction and a simulated image (thickness  $t = 40$  nm). (b–d) Polar-coordinate plots of peak intensity (radial direction), normalized by the intensity of cNP columns, measured from atom columns within the blue, green, and yellow hexagons illustrated in (a). (e,f) Analysis of reconstructed  $\text{Ni}_2\text{P}$  (colorful PUC and ETUC) on  $\text{Ni}_3\text{P}_3$ -terminated and  $\text{Ni}_4\text{P}_3$ -terminated  $\text{Ni}_5\text{P}_4$  (black PUC and ETUC). The green and pink circles denote the possibly reconstructed Ni and P atoms and the black arrows mark the unit-cell shift between the two structural phases.

conditions.<sup>35–37</sup> By comparing with the simulated image (the inset), we clearly see a sophisticated and less regular intensity distribution of atom columns on the experimental image, which is related to the presence of atomic terraces on the sample surface (Figure S2). According to our image simulations, the decreased contrast of collinear Ni/P (cNP) atom columns (blue circles) with increased specimen thickness positions the  $\text{Ni}_5\text{P}_4$  structural model on the experimental image (Figure S3). Furthermore, the six-fold-symmetric noncollinear Ni/P (ncNP) atom columns (marked by blue hexagons), with strong peak-intensity variations, exhibit a prominent reconstruction feature (Figure 2d). This is also hinted by asymmetric intensity feature of  $\langle 100 \rangle^*$  reflection spots in the selected area electron diffraction pattern with respect to the simulated one (Figure S1). For simplicity, positions of the ncNP columns are successively indexed as 0,

$\pi/3$ ,  $2\pi/3$ ,  $\pi$ ,  $4\pi/3$ , and  $5\pi/3$  points as illustrated in the structural model (Figure 2f). Particularly, it can be seen that the  $5\pi/3$ -point atomic columns (green circles) in the experimental image have the maximum peak intensity. For phosphorus (red circles) atoms bridged by noncollinear Ni2/Ni3 (ncNN) columns, the approximate peak intensities imply that surface atoms are not obviously reconstructed there.

By means of electron-beam bombardment to the  $\text{Ni}_5\text{P}_4$  nanosheets, we surprisingly found a thin layer of  $\text{Ni}_2\text{P}$  ( $\sim 3$  nm), which is characteristic of three-fold coordination of Ni to P atoms (Figure 2e). Being consistent with the EDX results, this suggests that the surfaces of  $\text{Ni}_5\text{P}_4$  nanosheets are coated by a thin layer of  $\text{Ni}_2\text{P}$ . Specifically, the observed  $\pi/6$  rotation of their primitive unit cells (PUCs) evidences their coherent epitaxy ( $a_{21} \approx \sqrt{3}a_{54}/2$ ) along the  $[001]$  direction (Figure 2f). The lattice parameters of the  $\text{Ni}_2\text{P}$  phase,  $a_{21} = 0.5859$  nm and

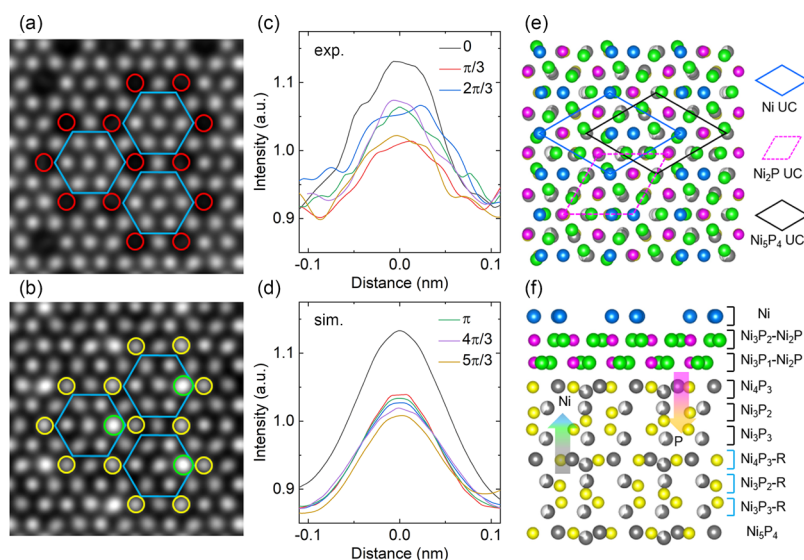


**Figure 4.** Surface chemical gradients unveiled by quantitative image simulations. (a) Simulated HAADF image of the Ni<sub>2</sub>P (2.2 nm)/Ni<sub>5</sub>P<sub>4</sub> (38.5 nm) bilayer along the [001] direction. (b) Simulated image of the Ni (1.9 nm)/Ni<sub>2</sub>P (2.2 nm)/Ni<sub>5</sub>P<sub>4</sub> (38.5 nm) triple-layer structure. The green and yellow circles denote the reconstructed Ni atoms at 0-point positions within the blue hexagons and at positions of pure P atoms in Ni<sub>5</sub>P<sub>4</sub>. (c,d) Intensity profiles of the ncNP columns within the blue hexagons from the experimental and simulated image, respectively. (e) Schematic plan view of the Ni/Ni<sub>2</sub>P/Ni<sub>5</sub>P<sub>4</sub> layered structure along the [001]<sub>54</sub> direction. (f) Schematic cross-sectional view of the Ni/Ni<sub>2</sub>P/Ni<sub>5</sub>P<sub>4</sub> layered structure along the [010]<sub>54</sub> direction. The arrows denote the diffusion direction of Ni and P in the multilayer structure.

$c_{21} = 0.3382 \text{ nm}$ ,<sup>38</sup> indicate that the self-epitaxial layer suffers a compressive strain  $\sim 0.3\%$  from the Ni<sub>5</sub>P<sub>4</sub> phase. From the overlapped structural models, we clearly see noncollinearity-induced elongation of most atom columns and several collinearly aligned columns along the viewing direction, for example, P atoms in Ni<sub>2</sub>P overlapped with the cNP atoms in Ni<sub>5</sub>P<sub>4</sub>. For describing their structural relationships in a simple way, the parallelogram PUCs of both phases are re-shaped into six-fold-symmetric equivalently transformed unit cells (ETUCs), respectively.

It is noteworthy that the reconstruction feature is also observed in our HAADF-STEM images of the HER-tested nanosheets, where the brightest ncNP atom columns within the blue hexagons appear at the 0-point positions (Figure 3a). A large-area image showing a uniform surface reconstruction of atoms at this position is presented in Figure S4. Since the image contrast of HAADF image is proportional to  $\sim Z^2$  ( $Z$  = atomic number),<sup>39</sup> the atoms with smaller  $Z$ , for example, P ( $Z$  = 15), O ( $Z$  = 8), and H ( $Z$  = 1), on the surface of the Ni<sub>5</sub>P<sub>4</sub> phase are therefore invisible owing to their weak-scattering ability to the incident electrons. Being consistent with the simulated image (inset in Figure 3a), this clearly signifies the reconstruction of heavy Ni ( $Z$  = 28) atoms on top of these P-occupying positions (red circles), which does not exclude the presence of surface species like H<sub>2</sub>O and PH<sub>x</sub>. With respect to the experimental image, we also noticed the absence of elongated ncNP atom columns in the simulated image. Furthermore, we see that the ncNN atom columns always have the strongest peak intensities.

Because the HAADF-STEM images mainly show signals from the heavy Ni atoms, the surface structure disclosed by this method, to a certain degree, decomposes the reconstruction feature manifested by the TEM results. For simplicity, the atomic surface reconstruction is hereafter deciphered through simulation-based measurement of the HAADF images. Referring to the peak intensity of the cNP columns (marked by blue circles), all column-peak intensities are measured and

plotted in polar coordinates. Within the blue hexagons (Figure 3b), the  $\pi/3$ - and  $5\pi/3$ -point columns have the lowest intensity, identical to the reference cNP column and the  $2\pi/3$ -,  $\pi$ -, and  $4\pi/3$ -point columns have an intermediate peak intensity. Within the neighboring green hexagon (Figure 3a,c), the 0-point ncNN columns and all ncNP columns have a stronger peak intensity than that of the reference column. Meanwhile, the 0-point ncNP column also has a stronger peak intensity than those of the  $2\pi/3$ - and  $4\pi/3$ -point columns within the orange hexagon (Figure 3d). In addition, the collinear P columns (yellow atoms and denoted by red circles) in the green and orange hexagons also have different peak intensities. In fact, the HAADF-STEM images also unveil a complex reconstruction feature of atoms on the phosphide surface.

To find out the origin of the surface reconstruction, the sublayer structural features of Ni<sub>5</sub>P<sub>4</sub> are analyzed along the [001] direction. Given their lattice match relationship, the (001)-oriented sublayers of Ni<sub>5</sub>P<sub>4</sub> are repartitioned by the ETUCs of Ni<sub>2</sub>P. It is surprisingly found that the Ni<sub>3</sub>P<sub>3</sub> sublayer is comprised of two kinds of ETUCs<sub>21</sub> (Figure 3e), periodic Ni<sub>3</sub>P<sub>2</sub> (orange hexagons) gapped by interconnected Ni<sub>2</sub>P<sub>7/3</sub> (green hexagons). Obviously, the Ni<sub>3</sub>P<sub>2</sub> hexagons provide a favorable condition for epitaxial growth of Ni<sub>2</sub>P on top of Ni<sub>5</sub>P<sub>4</sub>, and additional filling of Ni (green circles) and P (pink circles) atoms at certain positions may possibly happen at the (001) interface of the two phases. Analogously, the Ni<sub>4</sub>P<sub>3</sub> sublayer, comprising of Ni<sub>3</sub>P<sub>2</sub> (orange) and Ni<sub>3</sub>P<sub>7/3</sub> (green) ETUC<sub>21</sub>, may also be favorable for the epitaxial growth (Figure 3f). Nevertheless, the Ni<sub>3</sub>P<sub>2</sub> sublayer does not show features facilitating construction of Ni<sub>2</sub>P on top of Ni<sub>5</sub>P<sub>4</sub> (Figure S5).

Based on this, the atomic reconstructions on Ni<sub>5</sub>P<sub>4</sub> (001) surfaces were examined by image simulations, in which the Ni<sub>4</sub>P<sub>3</sub>-terminated Ni<sub>5</sub>P<sub>4</sub> was superimposed by a layer of Ni<sub>2</sub>P (Figure 4a). At the pure P-occupying positions, despite overlaying of Ni atoms in Ni<sub>2</sub>P on the top, clear column intensities can hardly be discerned from the simulated image.

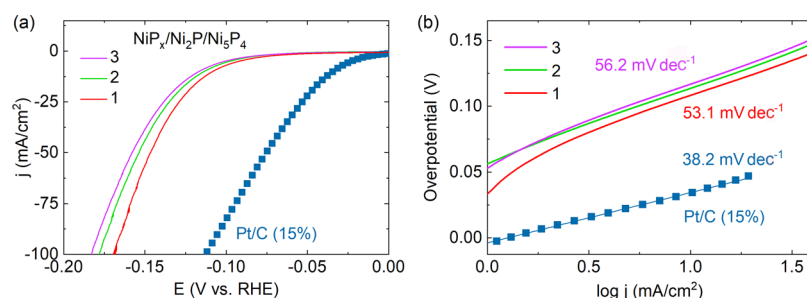


**Figure 5.** Catalytic performance of the heterostructure nanosheets measured in  $N_2$ -saturated 0.5 M  $H_2SO_4$ . (a) Polarization (LSV) curves and (b) Tafel plots measured before and after each 1000-cycle ADT with respect to the commercial Pt/C (15%) catalyst. The scan rate is  $5 \text{ mV s}^{-1}$ .

Only when an additional layer of Ni atoms is superimposed on top of  $Ni_2P$ , the prominent reconstruction features can be reproduced, for example, the column intensities at pure P-occupying positions and the 0-point ncNP within the blue hexagons (Figure 4b). Judging from the intensity profiles of the ncNP columns, our simulation suggests that thickness of the top-most Ni layer is about 2 nm (Figure 4c,d). It should be noted that the electron-channeling effects<sup>40</sup> also lead to intensity variations of the neighboring nonreconstructed columns. Meanwhile, the P atoms may also be involved in the surface atom reconstruction.

A schematic structure model corresponding to the simulated image is presented along the plan-view direction (Figure 4e). It can be seen that the reconstructed Ni atoms do not alter periodicity of the  $Ni_5P_4$  lattices. Therefore, the surface atom reconstruction is not manifested by the presence of superstructure spots in the selected area electron diffraction patterns (Figure S1). In addition, we found that the nickel atoms at specific sites ( $Ni_2$ ,  $Ni_3$ , and  $Ni_4$ ) of  $Ni_5P_4$  tend to be deficient (Figure 1a). This is evidenced by a dramatic intensity mismatch of the ncNN columns between the experimental and the simulated images of  $Ni_5P_4$  at an ideal stoichiometry (Figure 3a and inset). Without considering the nickel deficiencies, the ncNN columns always have the strongest intensities, leading to failure in reproducing the experimentally observed reconstruction features, even with overlapping of  $Ni_2P$  on the top (Figure S6). According to our image simulations, it is estimated that the occupation (Occ.) of nickel is  $Occ_{Ni_2} = Occ_{Ni_3} = 0.6$  and  $Occ_{Ni_4} = 0.8$  (Figure 4c). The structural parameters used for the image simulations are presented in Table S1.

With respect to the self-epitaxial hetero-nanolayers, the cationic vacancies identified in the  $Ni_5P_4$  phase reveal that the Ni atoms possess high thermodynamic activity. That is to say, during the phosphorization process,<sup>5</sup> which is under non-equilibrium thermal conditions, the Ni atoms diffuse quickly toward the exterior surfaces associated with an inverse diffusion of P atoms toward the interior (Figure 4f). This explains why the Ni tends to be enriched on the surfaces of the phosphides. It should be noted that the surface Ni atoms are not existing in an elemental form. Its valence in the range of 0–1, as detected by X-ray photoelectron spectroscopy (XPS) (Figure S7), shows that the Ni atoms may reconstruct together with the P atoms, which probably form a layer of  $NiP_x$  ( $0 < x < 0.5$ ) on the phosphide surfaces. Such a hetero-epitaxial scenario is further supported by complex reconstruction of  $NiP_x$  on surfaces of the  $Ni_2P$  nanosheets (Figure S8), which has an atomic ratio of  $Ni/P = 2.16 \pm 0.25$ .

Regarding the proportion of the  $Ni_2P$  phase in the  $Ni_xP_y$  nanosheets, our previous quantitative X-ray diffraction analysis reveals that it takes about 22% in the as-grown sample,<sup>5</sup> which decreases to  $\sim 18\%$  after the 72-h HER test in the  $N_2$ -saturated 0.5 M  $H_2SO_4$  electrolyte. According to our statistical observations, only a few (less than 5)  $Ni_2P$ -dominant nanosheets were identified among tens of them ( $\sim 50$ ). This suggests that most of the  $Ni_2P$  phase undergoes an epitaxial growth on surfaces of the  $Ni_5P_4$  phase. Assuming the  $Ni_2P/Ni_5P_4$  phase ratio is 1:4, for a nanosheet with a thickness of 10 or 100 nm, the thickness of the self-epitaxial  $Ni_2P$  phase is 2 or 20 nm, being consistent with our results presented in Figure 2e. The polarization curves with the  $iR$  correction (*i.e.*, electrolyte resistance compensation) for the heterogeneous nanosheets are measured and presented (Figure 5a). Compared with the 15% Pt/C catalyst, we see that an overpotential ( $\eta$ ) value of  $\eta = 108$ , 147, and 169 mV is required to achieve a current density ( $j$ ) of 10, 50, and 100  $\text{mA cm}^{-2}$ , respectively, for the as-grown nanosheets. After two accelerated degradation tests (ADTs), the overpotential individually increases to 117, 158, and 183 mV to achieve the same current densities. Correspondingly, a linear fitting to the  $\eta$  versus  $\log(j)$  relation reveals that the Tafel slope increases from 53.1 to 56.2  $\text{mV dec}^{-1}$ , whereas 38.2  $\text{mV dec}^{-1}$  for the Pt/C catalyst (Figure 5b).

Regarding the presence of the self-epitaxial hetero-nanolayers, this can be ascribed to the following reasons. First, because the nanosheets were formed by vapor phosphorization of the Ni foam, the obvious chemical gradients during the synthesis are not favorable for formation of single-phase nickel phosphides,<sup>6,41</sup> which are sensitive to the Ni/P atomic ratio of the precursors.<sup>31</sup> Second, given the coherent (001) planes of the sublayers of both phases, the high thermodynamic activity of nickel favors the self-epitaxy of  $Ni_2P$  on top of the  $Ni_5P_4$  phase. Third, the formation temperature of the  $Ni_2P$  phase is lower than that of the  $Ni_5P_4$  phase,<sup>5,41</sup> which is also a favorable condition for epitaxial growth of the former phase on top of the latter phase during the cooling procedure of sample preparation. Therefore, with respect to the composition–activity relation summarized in Table 1, particularly the P-rich  $Ni_5P_4$ , our results suggest that the passivated catalytic activity is possibly attributed to the surface reconstruction arising from the Ni enrichment. This also provides a reference for understanding the catalytic activity of other Ni-containing catalysts, for example,  $Ni_3P$ ,  $Ni_{12}P_5$ ,  $Ni_3S_2$ , and  $NiSe$ .<sup>7,42–44</sup>

## CONCLUSIONS

Our atomic-scale structural study reveals a self-epitaxial growth of  $Ni_2P$  and  $NiP_x$  ( $0 < x < 0.5$ ) nanolayers on top of the (001)-

oriented Ni<sub>3</sub>P<sub>4</sub> phase, which should passivate the intrinsic catalytic activity of the Ni<sub>3</sub>P<sub>4</sub> phase. Besides the structural driving force arising from the similarity of their sublayers, the self-epitaxy of heterogeneous nanolayers may also be influenced by the synthesis method, precursor, temperature factor, and so on. Particularly, the identified surface chemical gradient associated with the core–shell configuration, driven by the high thermodynamic activity of nickel, innovates our traditional understanding of surface microstructures of the nickel phosphides. Therefore, it is believed that the findings offer a new perspective to understand the performance of the transition-metal catalysts, for example, phosphides, sulfides, and selenides. It also highlights the importance of performing atomic-scale 3D characterization to better configure the structure–activity relationship in electrochemical energy conversion.

## ■ ASSOCIATED CONTENT

### SI Supporting Information

The Supporting Information is available free of charge at <https://pubs.acs.org/doi/10.1021/acsami.0c03154>.

Morphology and selected area electron diffraction of the Ni<sub>3</sub>P<sub>4</sub> nanosheets; atomic-terraces identified from the atomic-resolution TEM image; identification of the atom column positions by means of image simulations; large-field view of the atomic-scale surface reconstruction from the HAADF-STEM image; repartition of Ni<sub>3</sub>P<sub>2</sub> sublayers of the Ni<sub>3</sub>P<sub>4</sub> phase by the ETUCs of Ni<sub>2</sub>P; simulated HAADF-STEM images of the [001]-oriented Ni<sub>3</sub>P<sub>4</sub> phase with consideration of different Ni vacancies and overlapping of Ni<sub>2</sub>P directly on Ni<sub>3</sub>P<sub>4</sub>; XPS spectra of Ni 2p<sub>3/2</sub> before and after the HER test and enrichment of Ni identified from the [001]-oriented Ni<sub>2</sub>P phase (PDF)

## ■ AUTHOR INFORMATION

### Corresponding Author

Xian-Kui Wei – Ernst Ruska-Centre for Microscopy and Spectroscopy with Electrons, Forschungszentrum Jülich GmbH, Jülich 52428, Germany; [orcid.org/0000-0003-4320-1120](https://orcid.org/0000-0003-4320-1120); Email: [x.wei@fz-juelich.de](mailto:x.wei@fz-juelich.de)

### Authors

Dehua Xiong – International Iberian Nanotechnology Laboratory (INL), Braga 4715-330, Portugal; State Key Laboratory of Silicate Materials for Architectures, Wuhan University of Technology, Wuhan 430070, China; [orcid.org/0000-0002-4714-9019](https://orcid.org/0000-0002-4714-9019)

Lifeng Liu – International Iberian Nanotechnology Laboratory (INL), Braga 4715-330, Portugal; [orcid.org/0000-0003-2732-7399](https://orcid.org/0000-0003-2732-7399)

Rafal E. Dunin-Borkowski – Ernst Ruska-Centre for Microscopy and Spectroscopy with Electrons, Forschungszentrum Jülich GmbH, Jülich 52428, Germany

Complete contact information is available at: <https://pubs.acs.org/doi/10.1021/acsami.0c03154>

### Notes

The authors declare no competing financial interest.

## ■ ACKNOWLEDGMENTS

This work is supported by the European Union's Horizon 2020 research and innovation program through the CritCat Project under grant agreement no. 686053.

## ■ REFERENCES

- (1) Li, Y.; Dong, Z.; Jiao, L. Multifunctional Transition Metal-Based Phosphides in Energy-Related Electrocatalysis. *Adv. Energy Mater.* **2019**, *10*, 1902104.
- (2) Zou, X.; Zhang, Y. Noble metal-free hydrogen evolution catalysts for water splitting. *Chem. Soc. Rev.* **2015**, *44*, 5148–5180.
- (3) Wang, Y.; Kong, B.; Zhao, D.; Wang, H.; Selomulya, C. Strategies for developing transition metal phosphides as heterogeneous electrocatalysts for water splitting. *Nano Today* **2017**, *15*, 26–55.
- (4) Xiao, P.; Sk, M. A.; Thia, L.; Ge, X.; Lim, R. J.; Wang, J.-Y.; Lim, K. H.; Wang, X. Molybdenum phosphide as an efficient electrocatalyst for the hydrogen evolution reaction. *Energy Environ. Sci.* **2014**, *7*, 2624–2629.
- (5) Wang, X.; Kolen'ko, Y. V.; Bao, X.-Q.; Kovnir, K.; Liu, L. One-step synthesis of self-supported nickel phosphide nanosheet array cathodes for efficient electrocatalytic hydrogen generation. *Angew. Chem., Int. Ed.* **2015**, *54*, 8188–8192.
- (6) Wang, X.; Li, W.; Xiong, D.; Petrovykh, D. Y.; Liu, L. Bifunctional nickel phosphide nanocatalysts supported on carbon fiber paper for highly efficient and stable overall water splitting. *Adv. Funct. Mater.* **2016**, *26*, 4067–4077.
- (7) Laursen, A. B.; Wexler, R. B.; Whitaker, M. J.; Izett, E. J.; Calvino, K. U. D.; Hwang, S.; Rucker, R.; Wang, H.; Li, J.; Garfunkel, E.; Greenblatt, M.; Rappe, A. M.; Dismukes, G. C. Climbing the volcano of electrocatalytic activity while avoiding catalyst corrosion: Ni<sub>3</sub>P, a hydrogen evolution electrocatalyst stable in both acid and alkali. *ACS Catal.* **2018**, *8*, 4408–4419.
- (8) Ledendecker, M.; Krick Calderón, S.; Papp, C.; Steinrück, H.-P.; Antonietti, M.; Shalom, M. The synthesis of nanostructured Ni<sub>3</sub>P<sub>4</sub> films and their use as a non-noble bifunctional electrocatalyst for full water splitting. *Angew. Chem., Int. Ed.* **2015**, *54*, 12361–12365.
- (9) Popczun, E. J.; McKone, J. R.; Read, C. G.; Biacchi, A. J.; Wiltout, A. M.; Lewis, N. S.; Schaak, R. E. Nanostructured nickel phosphide as an electrocatalyst for the hydrogen evolution reaction. *J. Am. Ceram. Soc.* **2013**, *135*, 9267–9270.
- (10) Laursen, A. B.; Patraju, K. R.; Whitaker, M. J.; Retuerto, M.; Sarkar, T.; Yao, N.; Ramanujachary, K. V.; Greenblatt, M.; Dismukes, G. C. Nanocrystalline Ni<sub>3</sub>P<sub>4</sub>: a hydrogen evolution electrocatalyst of exceptional efficiency in both alkaline and acidic media. *Energy Environ. Sci.* **2015**, *8*, 1027–1034.
- (11) Stern, L.-A.; Feng, L.; Song, F.; Hu, X. Ni<sub>2</sub>P as a Janus catalyst for water splitting: the oxygen evolution activity of Ni<sub>2</sub>P nanoparticles. *Energy Environ. Sci.* **2015**, *8*, 2347–2351.
- (12) Xu, J.; Wei, X.-K.; Costa, J. D.; Lado, J. L.; Owens-Baird, B.; Gonçalves, L. P. L.; Fernandes, S. P. S.; Heggen, M.; Petrovykh, D. Y.; Dunin-Borkowski, R. E.; Kovnir, K.; Kolen'ko, Y. V. Interface engineering in nanostructured nickel phosphide catalyst for efficient and stable water oxidation. *ACS Catal.* **2017**, *7*, 5450–5455.
- (13) Oyama, S. T. Novel catalysts for advanced hydroprocessing: transition metal phosphides. *J. Catal.* **2003**, *216*, 343–352.
- (14) Calvino, K. U. D.; Laursen, A. B.; Yap, K. M. K.; Goetjen, T. A.; Hwang, S.; Murali, N.; Mejia-Sosa, B.; Lubarski, A.; Teeluck, K. M.; Hall, E. S.; Garfunkel, E.; Greenblatt, M.; Dismukes, G. C. Selective CO<sub>2</sub> reduction to C3 and C4 oxyhydrocarbons on nickel phosphides at overpotentials as low as 10 mV. *Energy Environ. Sci.* **2018**, *11*, 2550–2559.
- (15) Hernandez, A. B.; Ariga, H.; Takakusagi, S.; Kinoshita, K.; Suzuki, S.; Otani, S.; Oyama, S. T.; Asakura, K. Dynamical LEED analysis of Ni<sub>2</sub>P (0001)-1×1: Evidence for P-covered surface structure. *Chem. Phys. Lett.* **2011**, *513*, 48–52.

- (16) Wang, Z.; Heng, N.; Wang, X.; He, J.; Zhao, Y. Surface and morphology structure evolution of metal phosphide for designing overall water splitting electrocatalyst. *J. Catal.* **2019**, *374*, 51–59.
- (17) Wexler, R. B.; Martirez, J. M. P.; Rappe, A. M. Stable phosphorus-enriched (0001) surfaces of nickel phosphides. *Chem. Mater.* **2016**, *28*, 5365–5372.
- (18) Wexler, R. B.; Martirez, J. M. P.; Rappe, A. M. Active role of phosphorus in the hydrogen evolving activity of nickel phosphide (0001) surfaces. *ACS Catal.* **2017**, *7*, 7718–7725.
- (19) Wexler, R. B.; Martirez, J. M. P.; Rappe, A. M. Chemical pressure-driven enhancement of the hydrogen evolving activity of Ni<sub>2</sub>P from nonmetal surface doping interpreted via machine learning. *J. Am. Chem. Soc.* **2018**, *140*, 4678–4683.
- (20) Liu, P.; Rodriguez, J. A. Catalysts for hydrogen evolution from the [NiFe] hydrogenase to the Ni<sub>2</sub>P (001) surface: The importance of ensemble effect. *J. Am. Ceram. Soc.* **2005**, *127*, 14871–14878.
- (21) Li, Q.; Hu, X. First-principles study of Ni<sub>2</sub>P (0001) surfaces. *Phys. Rev. B: Condens. Matter Mater. Phys.* **2006**, *74*, 035414.
- (22) Li, H.; Tsai, C.; Koh, A. L.; Cai, L.; Contryman, A. W.; Frapapan, A. H.; Zhao, J.; Han, H. S.; Manoharan, H. C.; Abild-Pedersen, F.; Nørskov, J. K.; Zheng, X. Activating and optimizing MoS<sub>2</sub> basal planes for hydrogen evolution through the formation of strained sulphur vacancies. *Nat. Mater.* **2016**, *15*, 364.
- (23) Ye, G.; Gong, Y.; Lin, J.; Li, B.; He, Y.; Pantelides, S. T.; Zhou, W.; Vajtai, R.; Ajayan, P. M. Defects engineered monolayer MoS<sub>2</sub> for improved hydrogen evolution reaction. *Nano Lett.* **2016**, *16*, 1097–1103.
- (24) Kibsgaard, J.; Chen, Z.; Reinecke, B. N.; Jaramillo, T. F. Engineering the surface structure of MoS<sub>2</sub> to preferentially expose active edge sites for electrocatalysis. *Nat. Mater.* **2012**, *11*, 963–969.
- (25) Kibsgaard, J.; Jaramillo, T. F. Molybdenum phosphosulfide: an active, acid-stable, earth-abundant catalyst for the hydrogen evolution reaction. *Angew. Chem., Int. Ed.* **2014**, *53*, 14433–14437.
- (26) Chang, J.; Li, K.; Wu, Z.; Ge, J.; Liu, C.; Xing, W. Sulfur-doped nickel phosphide nanoplates arrays: a monolithic electrocatalyst for efficient hydrogen evolution reactions. *ACS Appl. Mater. Interfaces* **2018**, *10*, 26303–26311.
- (27) Liu, K.; Wang, F.; He, P.; Shifa, T. A.; Wang, Z.; Cheng, Z.; Zhan, X.; He, J. The role of active oxide species for electrochemical water oxidation on the surface of 3d-metal phosphides. *Adv. Energy Mater.* **2018**, *8*, 1703290.
- (28) Li, Z.; Dou, X.; Zhao, Y.; Wu, C. Enhanced oxygen evolution reaction of metallic nickel phosphide nanosheets by surface modification. *Inorg. Chem. Front.* **2016**, *3*, 1021–1027.
- (29) Hansen, M. H.; Stern, L.-A.; Feng, L.; Rossmesl, J.; Hu, X. Widely available active sites on Ni<sub>2</sub>P for electrochemical hydrogen evolution—insights from first principles calculations. *Phys. Chem. Chem. Phys.* **2015**, *17*, 10823–10829.
- (30) Kibsgaard, J.; Tsai, C.; Chan, K.; Benck, J. D.; Nørskov, J. K.; Abild-Pedersen, F.; Jaramillo, T. F. Designing an improved transition metal phosphide catalyst for hydrogen evolution using experimental and theoretical trends. *Energy Environ. Sci.* **2015**, *8*, 3022–3029.
- (31) Pan, Y.; Liu, Y.; Zhao, J.; Yang, K.; Liang, J.; Liu, D.; Hu, W.; Liu, D.; Liu, Y.; Liu, C. Monodispersed nickel phosphide nanocrystals with different phases: synthesis, characterization and electrocatalytic properties for hydrogen evolution. *J. Mater. Chem. A* **2015**, *3*, 1656–1665.
- (32) Jung, C. S.; Park, K.; Lee, Y.; Kwak, I. H.; Kwon, I. S.; Kim, J.; Seo, J.; Ahn, J.-P.; Park, J. Nickel phosphide polymorphs with an active (001) surface as excellent catalysts for water splitting. *CrystEngComm* **2019**, *21*, 1143–1149.
- (33) Barthel, J. Dr. Probe: A software for high-resolution STEM image simulation. *Ultramicroscopy* **2018**, *193*, 1–11.
- (34) Babizhetskyy, V.; Kotur, B.; Oryshchyn, S.; Zheng, C.; Kneidinger, F.; Leber, L.; Simson, C.; Bauer, E.; Michor, H. Crystal and electronic structure and physical properties of Ni<sub>3</sub>P<sub>4</sub>. *Solid State Commun.* **2013**, *164*, 1–5.
- (35) Jia, C. L.; Lentzen, M.; Urban, K. Atomic-resolution imaging of oxygen in perovskite ceramics. *Science* **2003**, *299*, 870–873.
- (36) Wei, X.-K.; Yang, Y.; McGilly, L. J.; Feigl, L.; Dunin-Borkowski, R. E.; Jia, C.-L.; Bellaiche, L.; Setter, N. Flexible polarization rotation at the ferroelectric/metal interface as a seed for domain nucleation. *Phys. Rev. B* **2018**, *98*, 020102.
- (37) Wei, X. K.; Jia, C. L.; Du, H. C.; Roleder, K.; Mayer, J.; Dunin-Borkowski, R. E. An unconventional transient phase with cycloidal order of polarization in energy-storage antiferroelectric PbZrO<sub>3</sub>. *Adv. Mater.* **2020**, *32*, 1907208.
- (38) Rundqvist, S.; Yhland, M.; Dahlbom, R.; Sjövall, J.; Theander, O.; Flood, H. X-ray investigations of Mn<sub>3</sub>P, Mn<sub>2</sub>P and Ni<sub>2</sub>P. *Acta Chem. Scand.* **1962**, *16*, 992.
- (39) Nellist, P. D.; Pennycook, S. J. The principles and interpretation of annular dark-field Z-contrast imaging. *Adv. Imaging Electron Phys.* **2000**, *113*, 147–203.
- (40) Haruta, M.; Kurata, H.; Komatsu, H.; Shimakawa, Y.; Isoda, S. Effects of electron channeling in HAADF-STEM intensity in La<sub>2</sub>CuSnO<sub>6</sub>. *Ultramicroscopy* **2009**, *109*, 361–367.
- (41) Li, J.; Li, J.; Zhou, X.; Xia, Z.; Gao, W.; Ma, Y.; Qu, Y. Highly efficient and robust nickel phosphides as bifunctional electrocatalysts for overall water-splitting. *ACS Appl. Mater. Interfaces* **2016**, *8*, 10826.
- (42) Huang, Z.; Chen, Z.; Chen, Z.; Lv, C.; Meng, H.; Zhang, C. Ni<sub>12</sub>P<sub>5</sub> Nanoparticles as an efficient catalyst for hydrogen generation via electrolysis and photoelectrolysis. *ACS Nano* **2014**, *8*, 8121–8129.
- (43) Yang, C.; Gao, M. Y.; Zhang, Q. B.; Zeng, J. R.; Li, X. T.; Abbott, A. P. In-situ activation of self-supported 3D hierarchically porous Ni<sub>3</sub>S<sub>2</sub> films grown on nanoporous copper as excellent pH-universal electrocatalysts for hydrogen evolution reaction. *Nano Energy* **2017**, *36*, 85–94.
- (44) Zou, Z.; Wang, X.; Huang, J.; Wu, Z.; Gao, F. An Fe-doped nickel selenide nanorod/nanosheet hierarchical array for efficient overall water splitting. *J. Mater. Chem. A* **2019**, *7*, 2233–2241.